

# TARS: Traffic-Aware Radar Scene Flow Estimation

Jialong Wu<sup>1,2</sup> Marco Braun<sup>2</sup> Dominic Spata<sup>2</sup> Matthias Rottmann<sup>1</sup>  
<sup>1</sup>University of Wuppertal <sup>2</sup>Aptiv Services Deutschland GmbH

## Abstract

Scene flow provides crucial motion information for autonomous driving. Recent LiDAR scene flow models utilize the rigid-motion assumption at the instance level, assuming objects are rigid bodies. However, these instance-level methods are not suitable for sparse radar point clouds. In this work, we present a novel **Traffic-Aware Radar Scene flow estimation method**, named TARS, which utilizes the motion rigidity at the traffic level. To address the challenges in radar scene flow, we perform object detection and scene flow jointly and boost the latter. We incorporate the feature map from the object detector, trained with detection losses, to make radar scene flow aware of the environment and road users. Therefrom, we construct a **Traffic Vector Field (TVF)** in the feature space, enabling a holistic traffic-level scene understanding in our scene flow branch. When estimating the scene flow, we consider both point-level motion cues from point neighbors and traffic-level consistency of rigid motion within the space. TARS outperforms the state of the art on a proprietary dataset and the View-of-Delft dataset, improving the benchmarks by 23% and 15%, respectively.

## 1. Introduction

Scene flow estimates a set of displacement vectors that capture point motion between two point cloud frames, supporting subsequent decision-making in autonomous driving.

Early point cloud scene flow methods typically extract point-level or point patch features [26, 39], then estimate the flow by aggregating neighboring information from two frames. Considering only point-level information can result in points from the same object moving in different directions with varying magnitudes [25]. Recent LiDAR scene flow methods focus on the rigid-motion assumption [15]: objects move rigidly without deformation; and a scene can be viewed as multiple rigidly moving objects and stationary parts. These LiDAR-based methods often begin with foreground segmentation, followed by clustering and matching to obtain instance pairs of the same object in two frames [17]. Then, they predict the rigid motion at the instance level for each object pair [11] or derive the instance-wise

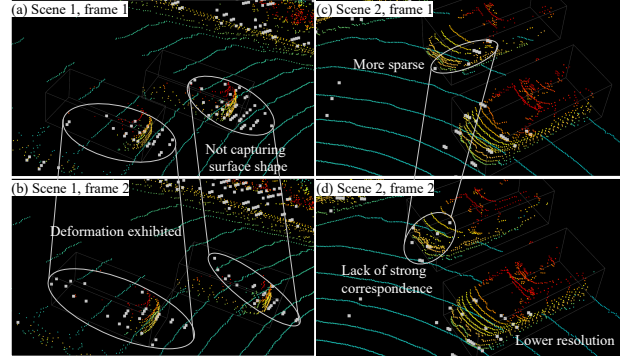


Figure 1. Challenges in radar scene flow. LiDAR point clouds are in color. The corresponding radar point clouds are shown in larger gray points. (a-b) and (c-d) are two pairs of consecutive frames.

transformation using optimization-based methods [16, 24].

However, these instance-level methods are not suitable for radar scene flow due to the inherent sparsity of radar data (cf. Fig. 1). Radar is more robust under different weather conditions and is typically an order of magnitude less expensive than LiDAR [36]. Nevertheless, radar points clouds are considerably sparser than LiDAR ones and do not capture object shapes. These challenges lead to a lack of reliable correspondences for matching instance pairs. Objects in radar point clouds may even exhibit deformations between frames due to the sparsity. Inferring rigid motion at the instance level may misinterpret such abnormal deformations as motion. Moreover, even nearby objects may have only a few reflection points (Fig. 1d), making optimization-based methods [24, 25] ineffective.

In this work, we focus on reconciling the contradiction between the rigid-motion assumption and the sparsity of radar point clouds. Although rigid motion of objects under radar is difficult to capture at the instance level, we believe this motion rigidity still exists within the space where the object locates. Therefore, we aim for a higher-level scene understanding, beyond the instance level, focusing on the traffic level to capture rigid motion hidden in the traffic context. When estimating the scene flow, we not only consider the motion cues propagated from neighboring points, but also consider the consistency of spatial context. This

still adheres to the rigid-motion assumption. In fact, previous methods also assume that motion rigidity exists in Euclidean space when performing clustering and paring of LiDAR points [15, 25]. However, to address the aforementioned challenges in radar scene flow, we do not further refine this assumption down to the instance level.

On the other hand, perceiving the environment and road users in the traffic is beneficial for motion prediction. Moreover, scene flow complements object detection with crucial motion information, enabling a more comprehensive perception. Therefore, we perform scene flow estimation and object detection jointly. We provide traffic cues to scene flow estimation through the object detector’s feature map, which has been trained with detection losses and contains all relevant features about road users and the environment.

In our network, we achieve the traffic-level scene understanding by building an traffic vector field (TVF). We define the TVF as: a discrete grid map that incorporates traffic information about road users and the environment, with each cell containing a vector representing the motion. A conceptual diagram is shown in Fig. 5b. Note that, we do not define an explicit 2D vector field; instead, we embed this concept within the feature space. The traffic information is extracted from the feature map of the object detection branch, and the motion information is passed through the hierarchical architecture of our scene flow branch. In each level of the architecture, we extract point-level motion cues from point neighbors while also paying attention to traffic-level motion consistency in Euclidean space. We use a coarse-grid TVF to achieve a high-level scene understanding, rather than falling into to point-level details.

We evaluate our model, TARS, on a proprietary dataset and the View-of-Delft (VOD) dataset [28]. Quantitative results demonstrate that TARS exceeds the state-of-the-art (SOTA) scene-flow accuracy on these datasets by 23% and 15 %, respectively. Radar scene flow heavily relies on the ability of radar sensors to capture object velocities. However, radar can only measure radial velocity, leading to significant underestimation of tangential motion. Qualitative results show that TARS effectively captures the rigid motion of objects while mitigating the tangential motion challenge.

Our main contributions are summarized as follows:

- We present TARS, the traffic-aware radar scene flow model that addresses the challenges of radar by leveraging the object detection feature map to obtain traffic context.
- We design the traffic vector field encoder and decoder module to encode traffic-level motion understanding into the TVF and capture rigid motion in Euclidean space.
- TARS clearly outperforms the SOTA accuracy by a large margin on both the proprietary dataset and VOD dataset.

## 2. Related Work

**Point cloud scene flow.** Scene flow for LiDAR point clouds has been widely studied over the past few years. Early methods [21, 26, 39], *e.g.* PointPWC-Net, use PointNet [30] as the point or patch feature extractor and calculate flow embeddings based on neighborhood information. Bi-PointFlowNet [6] uses the bidirectional flow embeddings to capture the motion context between frames. PV-RAFT [35] extracts point and voxel features to capture local and long-range correspondences. HALFlow [33] applies a double attention mechanism to aggregate information from neighbors. DeFlow [40] employs a gated recurrent unit (GRU) to transit voxel features to points and improves the efficiency on large-scale point clouds. Flow4D [20] fuses multiple frames into 4D voxels and extracts spatio-temporal feature. These methods infer scene flow only at the point patch level, without considering higher-level motion consistency.

WsRSF [15] and PCAccumulation [17] utilize the previously mentioned rigid-motion assumption at the instance level. They segment instance pairs and then regress the motion between each pair. Based on this approach, Dong et al. [11] introduce the nearest neighbor error minimization into a GRU to iteratively update the scene flow. Meanwhile, RigidFlow [24] uses the network output as the initialization for ICP (Iterative Closest Point) and refines the results. SCOOP [23] trains a pure correspondence model and computes scene flow via optimization with smoothness prior. Let-It-Flow [31] enforces rigidity in object clustering. MBNSF [32] encourages multi-body rigidity by adding a regularization term to the Chamfer loss. ICP-Flow [25] is a non-learning method using clustering to obtain instance pairs and a histogram-based approach to initialize ICP. As previously discussed, these methods designed for LiDAR, leveraging motion rigidity at the instance level, are unable to overcome the challenges in radar scene flow (Fig. 1).

**Radar scene flow.** Radar point cloud scene flow has only gained attention in recent years. MilliFlow [10] estimates human motion. RaFlow [8] employs motion segmentation and applies the Kabsch algorithm [18] to estimate the ego-motion transformation as the static flow. It treats the static points in the scene as a whole, but lacks a higher-level understanding of dynamic points. CMFlow [9] leverages additional cross-modal information as supervision signals to enhance the performance of radar scene flow. In this work, we provide additional traffic information for radar scene flow and capture the rigid motion of objects at the traffic level.

**Joint scene flow estimation & object detection.** Combining these two tasks enables a comprehensive perception in autonomous driving. Erçelik et al. [13] train a shared backbone with alternating task-specific heads, while PillarFlowNet [12] uses voxel representation and a multi-task head to jointly estimate scene flow and detect objects. PointFlowNet [4] further infers point-wise motion from

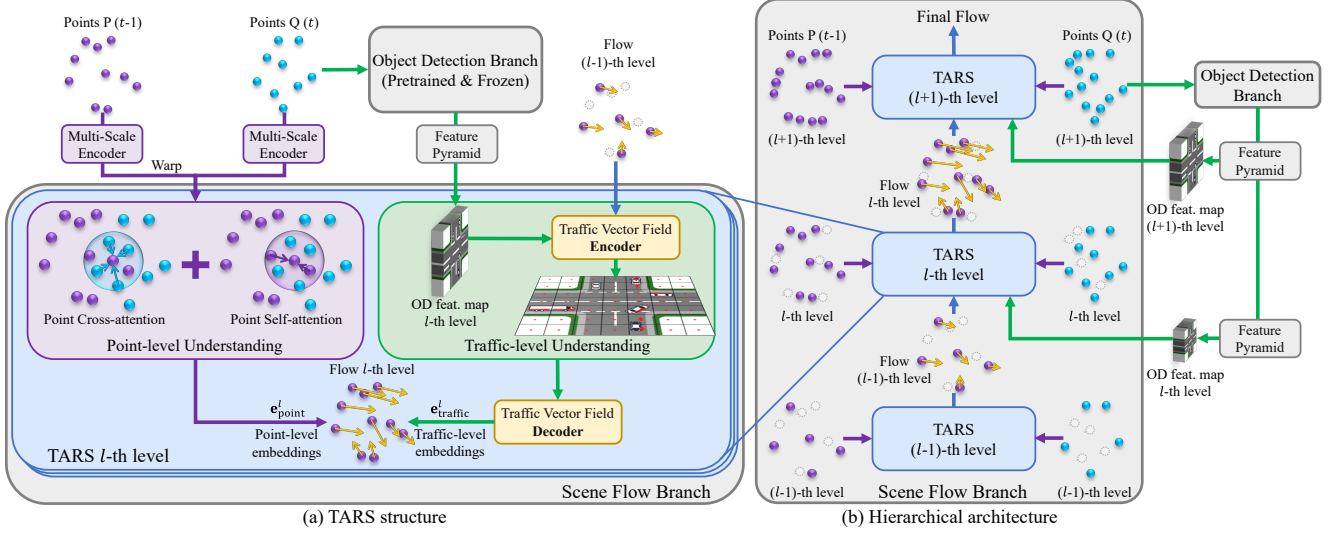


Figure 2. Overview of TARS. TARS employs a hierarchically architecture. At each level, it infers point-level motion cues using a double attention mechanism, while the TVF encoder leverages the OD feature map to build a traffic-level motion understanding. The TVF decoder captures the rigid motion that exists in Euclidean space. Finally, we use dual-level flow embeddings to estimate the scene flow.

voxels. These fine-grained voxel-based methods are limited to point patch-level motion understanding, with task interaction primarily on sharing backbone features. In contrast, our work provides a holistic traffic-level understanding for scene flow through synergistic interactions in the feature space. TrackFlow [19] directly derives LiDAR scene flow from object detection and tracking result. However, radar object tracking is significantly less accurate. Our approach perceives traffic context by leveraging feature maps, which reduces the reliance on object detection accuracy.

### 3. TARS Architecture

We introduce TARS in a top-down approach: starting with the hierarchical architecture that progressively refines scene flow (Sec. 3.1); then, using the  $l$ -th level as an example, we explain the structure of TARS and its dual-level motion understanding (Sec. 3.2). Thereafter, we dive into details of our TVF encoder, which encodes traffic and motion context into the TVF, achieving a traffic-level motion understanding (Sec. 3.3). The TVF decoder captures rigid motion hidden in the surrounding context, and the scene flow head combines point and traffic-level flow embeddings to predict the scene flow (Sec. 3.4). Finally, we briefly describe our recurrent module that leverages temporal cues (Sec. 3.5).

#### 3.1. Hierarchical Architecture

Following the hierarchical architecture in prior works [33, 39], TARS has  $L$  levels and predicts scene flow in a coarse-to-fine fashion, progressively refining the prediction. Perceiving the environment and road users in the traffic is beneficial for motion prediction, as they provide a traffic-

level motion prior. The object detection (OD) feature map, trained with detection losses, contains all relevant features about road users and the environment. Therefore, we jointly perform scene flow estimation and object detection (see Fig. 2b). We focus on enhancing the performance of radar scene flow, while the OD branch can be any detector, as long as it can generate bird’s-eye view feature maps to provide traffic information for the scene flow branch.

The input to our scene flow branch consists of two point clouds  $P \in \mathbb{R}^{N \times (3+2)}$  and  $Q \in \mathbb{R}^{M \times (3+2)}$ , with 5D initial features:  $x, y, z$  coordinates plus RRV (relative radial velocity) and RCS (radar cross-section) [42]. The multi-scale point encoder [30] is firstly applied to two point clouds for point feature extraction. Farthest point sampling is also performed to downsample the point clouds, yielding input point set pairs for each hierarchical level  $\{P^l \in \mathbb{R}^{N_l \times (3+C)}, Q^l \in \mathbb{R}^{M_l \times (3+C)}\}_{l=1}^L$ , where  $C$  is the extracted point feature dimensions,  $N_l$  and  $M_l$  are downsampled by a factor  $\gamma$ . Then, starting from the smallest point set, the  $(l-1)$ -th level of TARS computes flow embeddings  $\mathbf{e}^{l-1} \in \mathbb{R}^{N_{l-1} \times D}$  and generates a coarse scene flow  $F^{l-1} \in \mathbb{R}^{N_{l-1} \times 3}$ , which are then used as input for the next level. After refining the flow using multiple TARS levels, we obtain the final scene flow for the full point set.

From the second-lowest level, we boost scene flow estimation by incorporating traffic information from the OD branch (green arrows in Fig. 2b). Here, we feed the point cloud  $Q$  to the OD branch. The reason for using the feature map from  $Q$  rather than  $P$  is that: in our hierarchical architecture, the point cloud  $P$  is gradually warped to the corresponding positions in  $Q$  by each level’s flow prediction. Therefore, using  $Q$ ’s feature map allows for more accurate

alignment between points and object features.

### 3.2. TARS Structure

In radar scene flow, capturing motion rigidity at the instance level is challenging (cf. Fig. 1). However, we believe that rigid motion still exists within the space where the object locates. Therefore, with the help of the OD branch, we aim to achieve a traffic-level scene understanding to reveal the rigid motion hidden in the traffic context. Meanwhile, point-level matching information remains crucial for motion estimation. By integrating both point-level and traffic-level insights, TARS achieves a comprehensive motion understanding and enhances radar scene flow estimation.

Taking the  $l$ -th level as an example, Figure 2a shows the structure of TARS. The point-level understanding extracts motion cues from neighboring points, while the traffic-level understanding is achieved by building a TVF (defined in Sec. 1) to capture the motion consistency.

#### 3.2.1. Point-level motion understanding

Point motion can be inferred from the matching information between neighboring points across consecutive point cloud frames [39]. Previous studies [26, 39] use a multi-layer perceptron (MLP) to encode this point-level matching information, known as the cost volume, into the flow embeddings. However, we observed that these MLP-based methods are unstable in sparse radar point clouds, due to larger point spacing and fewer reflections per object. Therefore, we use a double attention mechanism to adaptively extract the matching information from radar point clouds.

For a point  $p_i^l \in \mathbb{R}^3$  in  $P^l$ , we compute cross-attention between  $p_i^l$  and its  $K$  nearest neighbors in  $Q^l$  (blue circle in Fig. 2a); then we apply self-attention between  $p_i^l$  and its neighboring points in  $P^l$  (purple circle in Fig. 2a). Unlike HALFlow [33], we remove the direction vector to mitigate the point spacing issue, and we employ heterogeneous keys and values to obtain fully attentive flow embeddings.

Specifically, we first warp the point cloud  $P^l$  closer to its neighbors in  $Q^l$  using the upsampled coarse flow from the previous level:  $P_{\text{warp}}^l = P^l + \text{Interp}(F^{l-1})$ . For simplicity, we omit this in the equations below. Let  $\mathbf{p}_i^l, \mathbf{q}_j^l \in \mathbb{R}^C$  represent the point features of  $p_i^l, q_j^l$ . We compute the cross-attentive matching embeddings  $\mathbf{e}_{\text{cross}}(p_i^l)$  for each point  $p_i^l$ :

$$\mathbf{e}_{\text{cross}}(p_i^l) = \text{Attention}(\mathbf{p}_i^l, \mathcal{N}_Q(p_i^l), \mathcal{N}_Q(p_i^l)), \quad (1)$$

$$\text{Attention}(\cdot, \diamond, \star) = \text{softmax}\left(\frac{\mathbf{Q}(\cdot)\mathbf{K}(\diamond)^T}{\sqrt{d_k}}\right)\mathbf{V}(\star), \quad (2)$$

where  $\mathcal{N}_Q(p_i^l) = \text{KNN}(p_i^l, Q^l)$  representing the  $K$  nearest neighbors of  $p_i^l$  in  $Q^l$ ;  $\mathbf{Q}(\cdot), \mathbf{K}(\cdot), \mathbf{V}(\cdot)$  are linear layers.

Then, the point-level flow embeddings  $\mathbf{e}_{\text{point}}(p_i^l)$  for a point  $p_i^l$  is computed via self-attention as:

$$\mathbf{e}_{\text{point}}(p_i^l) = \text{Attention}(\mathbf{e}_{\text{cross}}(p_i^l), \mathcal{N}_e(p_i^l), \mathcal{N}_e(p_i^l)), \quad (3)$$

where  $\mathcal{N}_e(p_i^l) = \text{KNN}(p_i^l, \mathbf{e}_{\text{cross}})$  fetches the matching embeddings for the neighbors of  $p_i^l$  in  $P^l$ .

#### 3.2.2. Traffic-level scene understanding

Our goal is to reconcile the rigid-motion assumption with the sparsity of radar point clouds. Instead of applying this assumption at the instance level [15, 25], we capture the rigid motion at the traffic level to address the challenges in radar. To achieve this, we design a TVF encoder that builds a traffic-level scene understanding. Then we employ a TVF decoder to capture rigid motion hidden in the traffic context.

Specifically, the feature map  $\chi_{\text{od}}^l$  from the OD branch contains traffic information, and the flow embeddings  $\mathbf{e}^{l-1}$  passed from the previous level carry motion information. The TVF encoder combines and encodes them into a coarse-grid TVF in the feature space, enabling traffic-level scene understanding (green & blue arrows in Fig. 2a). The TVF decoder employs cross-attention between points and TVF grids to perceive rigid motion and generate the traffic-level flow embeddings. In the TVF encoder, we apply global attention to build a holistic traffic-level understanding within the TVF. In contrast, the TVF decoder restricts the cross-attention to a local area, which helps to capture the rigid motion in spatial context. Finally, we combine point-level  $\mathbf{e}_{\text{point}}$  and traffic-level flow embeddings  $\mathbf{e}_{\text{traffic}}$  to enhance scene flow estimation (purple & green arrows in Fig. 2a).

### 3.3. Traffic Vector Field Encoder

Our TVF encoder integrates traffic and motion information into the TVF, and it progressively updates this traffic-level motion representation across TARS's hierarchical levels.

To this end, the TVF encoder employs two stages: (i) **scene update**: A GRU [1] leverages the OD feature map to update the TVF from the previous level; (ii) **flow painting**: Point-to-grid self-attention adaptively paints the coarse flow from the previous level onto the scene representation. Finally, we generate the new TVF  $\in \mathbb{R}^{H \times W \times D_{\text{TVF}}}$  using global attention. Figure 3 illustrates these two stages. The TVF maintains the same shape across each level and is configured to a coarse grid, e.g.  $2\text{m} \times 2\text{m}$ , enabling a high-level scene understanding without falling into point-level details. **Scene update**. In this stage, we update the scene representation by leveraging traffic features, from the  $l$ -th level of the OD feature pyramid, to refine the previous level's TVF $^{l-1}$ .

First, we apply CNN and pooling layers to the feature map  $\chi_{\text{od}}^l$  to adapt the object features and match the pre-defined shape of the coarse TVF. Then we use  $\chi_{\text{od}}^l$  as the input to a GRU, with TVF $^{l-1}$  as the hidden state. The GRU is applied in an inter-level manner for updating the scene representation  $\mathbf{X}_{\text{traffic}}^l$  across hierarchical levels:

$$\tilde{\mathbf{X}}_{\text{traffic}}^l = \tanh(\mathbf{W}_G * \chi_{\text{od}}^l + \mathbf{U}_G * (\mathbf{r}^l \odot \text{TVF}^{l-1})), \quad (4)$$

$$\mathbf{X}_{\text{traffic}}^l = \mathbf{z}^l \odot \text{TVF}^{l-1} + (1 - \mathbf{z}^l) \odot \tilde{\mathbf{X}}_{\text{traffic}}^l, \quad (5)$$



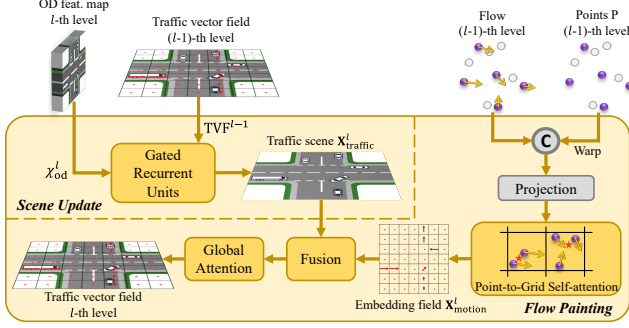


Figure 3. TVF encoder. Scene update: updates traffic information on the TVF using GRU; Flow painting: incorporates motion information into the TVF and build a holistic traffic representation.

where  $*$  is the convolution operation,  $\odot$  is the element-wise multiplication,  $\mathbf{W}_G, \mathbf{U}_G$  are 2D convolution kernels,  $\mathbf{r}^l, \mathbf{z}^l$  are the reset and update gates, for details we refer to [1].

**Flow painting.** In this stage, we project the coarse flow from the previous level onto the grid, using point-to-grid self-attention. Next, we fuse the motion representation with the scene representation and apply global attention to build a high-level scene understanding.

Specifically, we concatenate the  $(l-1)$ -th level’s flow embeddings  $\mathbf{e}^{l-1}$  with the point features  $\mathbf{p}^{l-1}$  extracted by the multi-scale encoder, and then project them onto the pre-defined 2D grid. Given that our TVF grid is coarse, each cell may contain multiple points with varying motion patterns (see Fig. 3). Therefore, we apply point-to-grid self-attention to adaptively extract motion features. We perform both channel-wise and point-wise self-attention within each grid cell and obtain the motion embedding field  $\mathbf{X}_{\text{motion}}^l$ .

After that, we fuse the traffic feature  $\mathbf{X}_{\text{traffic}}^l$  and motion feature  $\mathbf{X}_{\text{motion}}^l$  using spatial attention [38]. Briefly, we concatenate the two feature maps and process them through CNN layers followed by a pixel-wise softmax to generate spatial attention weights. The fused traffic-level feature  $\mathbf{X}_{\text{fusion}}^l$  is obtained as a weighted sum of  $\mathbf{X}_{\text{traffic}}^l$  and  $\mathbf{X}_{\text{motion}}^l$ .

Building high-level scene understanding should not be limited to local areas; a global receptive field is crucial for uncovering relationships among the motions of rigid bodies in traffic, *e.g.* the motion patterns of vehicles in the same lane. We use axial attention [34] to provide the global vision and build the traffic-level motion understanding. It splits a standard attention block into separate row-wise and column-wise components, reducing complexity yet preserving global context. By stacking  $\omega$  axial attention blocks, we enhance the fused features  $\mathbf{X}_{\text{fusion}}^l$  and obtain the final TVF $^l$ .

### 3.4. TVF Decoder & Scene Flow Head

Although radar point clouds are sparse, motion rigidity persists in Euclidean space. When building the traffic-level motion understanding, we encoded the rigid motion cues

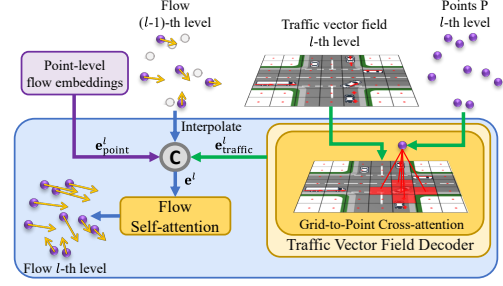


Figure 4. TVF decoder & scene flow head: capture motion rigidity in spatial context; combine dual-level embeddings for prediction.

into the coarse-grid TVF. Therefore, we use the TVF decoder to perceive rigid motion hidden in the traffic context.

Specifically, we apply grid-to-point cross-attention between each point  $p_i^l$  and its surrounding traffic context in the TVF, thereby integrating rigid motion cues into the flow embedding. To focus on relevant local rigid motion, the attentive receptive field is restricted to the nearby region around each point (see Fig. 4). We interpolate the coarse flow embeddings  $\mathbf{e}^{l-1}$  and concatenate with the point feature  $\mathbf{p}^l$  as the query, and the TVF grids as keys and values. This enables the resulting traffic-level flow embeddings  $\mathbf{e}_{\text{traffic}}(p_i^l)$  to be aware of motion consistency in the traffic context:

$$\hat{\mathbf{p}}_i^l = \text{Concat}(\text{Interp}(\mathbf{e}^{l-1})_i, \mathbf{p}_i^l), \quad (6)$$

$$\mathbf{e}_{\text{traffic}}(p_i^l) = \text{Attention}(\hat{\mathbf{p}}_i^l, \mathcal{N}_{\text{TVF}}(p_i^l), \mathcal{N}_{\text{TVF}}(p_i^l)), \quad (7)$$

where  $\mathcal{N}_{\text{TVF}}(p_i^l) = \text{KNN}(p_i^l, \text{TVF}^l)$  fetches the surrounding  $K$  cells of  $p_i^l$  from TVF $^l$ .

Combining point-level and traffic-level motion understanding, we obtain the final flow embeddings  $\mathbf{e}^l = \text{Concat}(\mathbf{e}_{\text{point}}, \mathbf{e}_{\text{traffic}}, \text{Interp}(\mathbf{e}^{l-1}))$ . Finally, we apply another self-attention as in Eq. (3) on  $\mathbf{e}^l$ , then reduce it back to  $C$  channels and produce the final scene flow  $F^l$ .

### 3.5. Temporal Update Module

Recurrent layers can leverage long-range temporal information to enhance radar scene flow. CMFlow uses a GRU to retain flow embeddings across frames; this slightly decreases the accuracy [9]. In contrast, we employ PointGRU layers [14] between frames as the temporal module (distinct

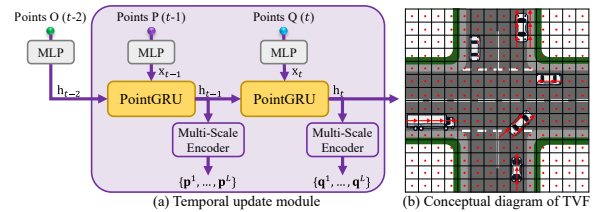


Figure 5. (a) Temporal update module: leverages low-level point dependencies using PointGRU. (b) Conceptual diagram of TVF.

from TVF encoder’s inter-level GRU) to capture dependencies in low-level point features. We store the point features of point cloud  $O$  at time  $t - 2$  as the hidden state and also update between the current point pairs (see Fig. 5a). During training we use sequences of  $T$  frames as mini-clips.

## 4. Experiments

### 4.1. Experiment Setup

**Dataset.** We conducted experiments on the View-of-Delft (VOD) dataset [28] and a proprietary dataset. Both datasets provide data from multiple sensors, including radar, LiDAR, camera, and GPS/IMU-based odometer. The VOD dataset contains mainly urban traffic scenes and is recorded using a low-resolution 4D radar, with each frame consisting of around 256 radar points. The VOD dataset includes 4662 training samples and 2724 test samples. The proprietary dataset is a  $20\times$  larger (in terms of frames) and more complex dataset. It contains 107,382 training samples and 24,198 test samples, covering urban, sub-urban, and highway scenes. It is collected by multiple high-resolution radars, after merging, around 6,000 radar points per frame.

**Metrics.** On the VOD dataset, we adopt the evaluation metrics from CMFlow [9]: 1. *EPE*: mean end-point-error ( $L_2$  distance) between the ground truth (GT) and the predicted scene flow. 2. *AccS/AccR*: Strict/Relaxed Accuracy, the percentage of points with  $EPE < 0.05/0.1$  m or a relative error  $< 5\%/10\%$ . 3. *RNE*: resolution normalized EPE, to accommodate low-resolution radar. 4. *MRNE* and *SRNE*: RNE computed separately for moving and static points.

The proprietary dataset is recorded by radars with higher resolution. Thus, we do not use RNE. Since moving objects are more critical in real-world autonomous driving, we focus on the accuracy of moving points. For moving points, we measure the following: 1. *MEPE*: *EPE* of moving points. 2. *MagE* and 3. *DirE*: magnitude and direction error between the GT and prediction. 4. *AccS/AccR* of moving points. For static points, we only calculate 5. *SEPE*; and we use 6. *AvgEPE*, the mean of MEPE and SEPE, as an overall metric. Metric details are provided in Appendix D.1.

### 4.2. Implementation Details

**Model details.** The hyperparameters for both datasets are listed in Tab. 1. TARS has 4 levels, which is not displayed in previous diagrams for simplicity. Since the VOD dataset has only 256 points per frame, we do not perform downsampling. Our TVF uses a coarse grid to gain a high-level understanding rather than confined to point-level details. On VOD dataset, we use the Adam optimizer with a learning rate  $10^{-3}$ , a decay rate of 0.9 per epoch, training for 60 epochs. On the proprietary dataset, which is  $20\times$  larger, we set the learning rate to  $10^{-4}$  with a decay of 0.8 per 30K steps and train for 3 epochs. In the Appendix, we provide

Table 1. Params for two datasets.  $L, N, M, T$ : number of levels, points or mini-clips.  $\gamma$ : downsampling factor.  $C, D, D_{TVF}$ : feature channels of points, flow embeddings, and TVF.  $\omega$ : number of axial attention blocks.  $\mathcal{N}_Q, \mathcal{N}_{TVF}$ : KNN points or TVF cells. TVF grid:  $[H, W]$  and size of TVF. ego-info: availability of ego-motion.

Dataset	$L$	$N, M$	$\gamma$	$C$	$D$	$D_{TVF}$	$\omega$	$\mathcal{N}_Q$	$\mathcal{N}_{TVF}$	$T$	TVF grid	ego-info
VOD	4	256	1	64	256	128	4	16	9	5	[40,40] 1.28m	Sup.
proprietary	4	6K	2	64	256	128	4	8	9	12	[70,40] 2.0m	Input

details and ablation studies of the OD branch (A.6, B.1), runtime analysis (C), and dual-task training strategy (A.5).

On the proprietary dataset, we simulate real-world autonomous driving by providing **all** tested models with ego-motion  $\Omega \in \mathbb{R}^{4 \times 4}$  from the GPS/IMU sensor as known input. We apply ego-motion compensation to align  $P$  and  $Q$  into the same coordinate system. In this case, the GT for static points is the zero vector. On the VOD dataset, we test our model under two setups: (i) **TARS-ego**: following CMFlow [9], using the ego-motion transformation to train an additional ego-motion head for a fair comparison; (ii) **TARS-superego**: using ego-motion as known input and applies compensation, same as on the proprietary dataset. Details of the setups please see Appendix A.2 and A.3.

**Weakly-supervised training.** Since annotating scene flow is extremely difficult, we follow the self-supervised losses in [8] and cross-modal losses in [9], and additionally employ a new loss for static points. Due to page constraints, we present a brief overview of the losses here; for further details, please refer to Appendix D.2. On both datasets, we apply the following losses: 1. soft Chamfer loss  $\mathcal{L}_{sc}$ : aligns  $P_{warp}$  and  $Q$  by minimizing distances between nearest points while handling outliers using probabilistic matching; 2. spatial smoothness loss  $\mathcal{L}_{ss}$ : enforces neighboring points to have similar flow vectors, weighted by distance to ensure spatial smoothness; 3. radial displacement loss  $\mathcal{L}_{rd}$ : constrains the radial projection of predicted flow vectors using radar’s RRV measurements; 4. foreground loss  $\mathcal{L}_{fg}$ : derives the pseudo scene flow GT from a LiDAR multi-object tracking model, applying to the predicted flow  $F_{fg}^l$  of foreground moving points at each level; 5. additionally, we employ a background loss  $\mathcal{L}_{bg}$ : using the ego-motion transformation as pseudo GT  $\hat{F}_{bg}^l$  for static points at each level:

$$\mathcal{L}_{bg}^l = \frac{1}{N_{bg}^l} \sum_{i=1}^{N_{bg}^l} \left\| \hat{f}_{bg_i}^l - f_{bg_i}^l \right\|_2, \quad (8)$$

$$\mathcal{L}_{all} = \mathcal{L}_{sc} + \mathcal{L}_{ss} + \mathcal{L}_{rd} + \sum_{l=1}^L (\mathcal{L}_{fg}^l + \lambda_{bg} \mathcal{L}_{bg}^l), \quad (9)$$

where  $\mathcal{L}_{all}$  is the overall loss, background weight  $\lambda_{bg} = 0.5$ .

For training TARS-ego on VOD dataset, we add cross-modal losses [9]: the motion segmentation loss  $\mathcal{L}_{seg}$ : using the pseudo segmentation GT (from odometer and RRV measurements) to train a motion-segmentation head; the ego-motion loss  $\mathcal{L}_{ego}$ : using the GT ego-motion to train an ego-

Table 2. Scene flow evaluation on the VOD dataset. Mean metric values across the test set are reported. “Sup.” indicates the supervision signal, Self: training with only self-supervised losses [8], Cross: with additional cross-modal losses [9], Cross<sup>+</sup>: setup for TARS-superego, without  $\mathcal{L}_{\text{seg}}$ ,  $\mathcal{L}_{\text{ego}}$ , and  $\mathcal{L}_{\text{opt}}$  while using ego-motion  $\Omega$  as known input for ego-motion compensation, same as on the proprietary dataset.

Method	Sup.	Overall				Moving	Static
		EPE [m]↓	AccS [%]↑	AccR [%]↑	RNE [m]↓	MRNE [m]↓	SRNE [m]↓
PointPWC-Net [39]	Self	0.422	2.6	11.3	0.169	0.154	0.170
SLIM [3]	Self	0.323	5.0	17.0	0.130	0.151	0.126
FlowStep3D [21]	Self	0.292	3.4	16.1	0.117	0.130	0.115
Flow4D-2frame [20]	Cross	0.255	10.0	26.2	0.103	0.125	0.098
RaFlow [8]	Self	0.226	19.0	39.0	0.090	0.114	0.087
DeFlow [40]	Cross	0.217	11.8	31.6	0.087	0.098	0.085
CMFlow [9]	Cross	0.130	22.8	53.9	0.052	0.072	0.049
TARS-ego (ours)	Cross	<b>0.092 (-0.038)</b>	<b>39.0 (+16.2)</b>	<b>69.1 (+15.2)</b>	<b>0.037 (-0.015)</b>	<b>0.061 (-0.011)</b>	<b>0.034 (-0.015)</b>
TARS-superego (ours)	Cross <sup>+</sup>	<b>0.048</b>	<b>76.6</b>	<b>86.4</b>	<b>0.019</b>	<b>0.057</b>	<b>0.014</b>

Table 3. Scene flow evaluation on the proprietary dataset. Mean metric values across the test set are reported. Ego-motion compensation is applied to **all** models for a fair comparison. PointGRU is applied in all models except for the one in the first row.

Method	PointGRU	Moving					Overall	Static
		MEPE [m]↓	MagE [m]↓	DirE [rad]↓	AccS [%]↑	AccR [%]↑	AvgEPE [m]↓	SEPE [m]↓
PointPWC-Net [39]	✗	0.453	0.363	1.218	44.2	52.2	0.244	0.036
PointPWC-Net [39]	✓	0.213	0.178	0.762	49.0	60.5	0.124	<b>0.035</b>
HALFlow [33]	✓	0.170	0.135	0.721	50.9	63.8	0.104	0.038
TARS (ours)	✓	<b>0.069 (-0.101)</b>	<b>0.059 (-0.076)</b>	<b>0.599 (-0.122)</b>	<b>69.8 (+18.9)</b>	<b>86.8 (+23.0)</b>	<b>0.054 (-0.05)</b>	0.038

motion head; and the optical flow loss  $\mathcal{L}_{\text{opt}}$ : projecting the scene flow onto an image and training with pseudo optical flow labels. For further details, please see Appendix D.2.

### 4.3. Comparison with State of the Art

**Experiments on the VOD dataset.** We compare our model TARS with the SOTA scene flow methods on the VOD dataset (see Tab. 2). The supervision signals are explained in the caption. TARS clearly outperforms the previous best model CMFlow [9] across all evaluation metrics in both setups. Under the same setup as CMFlow, our TARS-ego reduces the overall EPE from 0.13m to 0.092m, marking a 0.038m reduction and achieving a new milestone by bringing EPE below the AccR threshold of 0.1m. Moreover, TARS-ego improves AccS and AccR, two accuracy metrics computed based on EPE, by 16.2% and 15.2%, respectively. RNE is computed as  $RNE = \frac{EPE}{r_R/r_L}$ , where  $\frac{r_R}{r_L}$  is the ratio between radar and LiDAR resolution, averaging 2.5. Therefore, reductions in RNE metrics are numerically smaller. Nevertheless, TARS-ego shows substantial improvements in all three RNE-related metrics. We also compare TARS-ego with latest LiDAR models [20, 40]. These models perform worse because their fully-voxel representation, designed for large-scale LiDAR point clouds, are unsuitable for radar scene flow. Ego-motion from the odometer is a simple (just a  $\mathbb{R}^{4 \times 4}$  matrix) yet effective booster. Assuming real-world autonomous driving with an available odometer, TARS-superego applies ego-motion compensation and reduces the EPE down to 0.048m, MRNE to 0.057m, and boosts AccS and AccR to 76.6% and 86.4%, respectively.

**Experiments on the proprietary dataset.** The proprietary dataset is more complex, including high-speed scenarios such as highways and suburban scenes, which make radar scene flow estimation particularly challenging. There-

Table 4. Ablation study on the proprietary dataset. PointLevel: point-level motion understanding. ODFeatmap: using OD feature map. CoarseGrid: using coarse-grid TVF. GlobAttn: global attention applied. The chosen setup of TARS is highlighted in blue.

No.	Point Level	OD Featmap	Coarse Grid	Glob Attn	Moving			Overall	Static
					MEPE↓	AccS↑	AccR↑	AvgEPE↓	SEPE↓
1	✓				0.178	47.9	61.6	0.106	0.033
2	✓	✗	✓	✓	0.144	45.0	63.3	0.093	0.041
3	✓	✓	✗	✓	0.104	51.4	69.9	0.076	0.049
4	✓	✓	✓	✗	0.074	65.6	84.2	<b>0.053</b>	<b>0.031</b>
5	✓	✓	✓	✓	<b>0.069</b>	<b>69.8</b>	<b>86.8</b>	0.054	0.038
6		Decoder $\mathcal{N}_{\text{TVF}} = 5$			0.071	67.2	86.5	0.064	0.057
7		Decoder $\mathcal{N}_{\text{TVF}} = 9$			<b>0.069</b>	<b>69.8</b>	<b>86.8</b>	<b>0.054</b>	<b>0.038</b>
8		Decoder $\mathcal{N}_{\text{TVF}} = 13$			0.077	59.9	84.0	0.060	0.043

fore, to simulate real-world autonomous driving, we apply ego-motion compensation to **all** tested models and focus on moving points during evaluation (see Tab. 3). Furthermore, we add our temporal update module (Sec. 3.5) to other models for a fair comparison. Our model TARS outperforms the previous best model HALFlow [33] by a large margin, reducing MEPE from 0.17m to 0.069m and improving AccS and AccR by 18.9% and 23%, respectively. Qualitative results in Fig. 6 show that TARS effectively captures the rigid motion of radar points on the same object and mitigates the tangential motion challenge mentioned in Sec. 1.

### 4.4. Ablation Study

**Importance of key components.** We demonstrate the effectiveness of the key components of TARS on the proprietary dataset. Ablation study *No. i* refers to the *i*-th row of Tab. 4. *No. 1*: We completely remove the traffic level, causing the model to degrade to inferring motion cues solely at the point level, resulting in MEPE of 0.178m, close to HALFlow (Tab. 3). *No. 2*: We activate the traffic level but without the OD feature map, meaning no scene update is performed in the TVF encoder. This degrades our model to

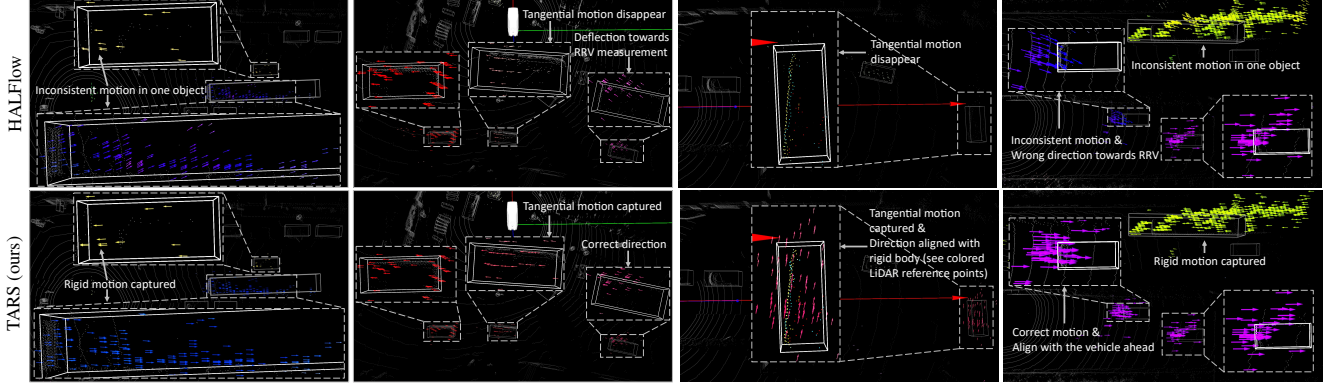


Figure 6. Qualitative results on the proprietary dataset, compared with HALFlow [33]. LiDAR point clouds serve as reference. Arrows indicate the predicted scene flow. After ego-motion compensation, static points are expected to yield zero vectors if predicted correctly. By perceiving traffic-level motion cues, TARS effectively captures the rigid motion in Euclidean space, as well as tangential movements.

simply combining point- and voxel-based motion features, leading to unsatisfactory AccR of 63.3%. *No. 3*: We enable the OD feature map and scene update, but change the coarse grid of TVF to a fine grid, from  $2m \times 2m$  to  $1m \times 1m$  with shape [140, 80]. In this case, our traffic-level understanding falls into point-level details, resulting in a reduction of MEPE by 0.04m, yet the improvement in accuracy is limited (AccR 69.9%). *No. 4*: We apply a coarse TVF to achieve high-level understanding, which further reduces MEPE by 0.03m and boosts the accuracy; but we replace the global attention in the TVF encoder with local convolutions. This makes the TVF focus on local areas, achieving the lowest SEPE of 0.031m, while limiting its ability to capture global traffic information (e.g., motion of vehicles in the same lane). *No. 5*: We construct a holistic traffic model using global attention. Compared to No. 4, this improves AccS by 4.2% and AccR by 2.6%. Although SEPE increased, all models maintain a low SEPE (below 0.05m) due to ego-motion compensation, and we prioritize dynamic objects in autonomous driving. *No. 6-8* show the effect of  $\mathcal{N}_{TVF}$ : the number of TVF cells that a point query attends to, when capturing motion context. In the cross-attention, considering more spatial context  $\mathcal{N}_{TVF} = 9$  (surrounding neighbors) improves AccS by 2.6% and reduces SEPE by 0.019m, compared to  $\mathcal{N}_{TVF} = 5$  (only direct neighbors). However, expanding to  $\mathcal{N}_{TVF} = 13$  (second-order neighbors) increases SEPE and significantly reduces AccS, due to the inclusion of irrelevant parts in the attention. Besides, on PointPWC-Net in Tab. 3, we demonstrate the importance of applying PointGRU to utilize temporal information.

**Effect of losses.** We evaluate the effects of losses on the VOD dataset (Tab. 5). Group *No. 1*: We test the impact of the proposed background loss  $\mathcal{L}_{bg}$  using a TARS-no-ego model, which excludes the ego-motion head of TARS-ego as well as three losses  $\mathcal{L}_{seg}$ ,  $\mathcal{L}_{ego}$ , and  $\mathcal{L}_{opt}$ . The experiments show that setting the background weight  $\lambda_{bg} = 0.5$  results in the lowest MRNE of moving points. Further increasing

Table 5. Ablation study on the VOD dataset. TARS-no-ego: without ego-motion head and supervision signals  $\mathcal{L}_{\{seg, ego, opt\}}$ . The chosen setup of TARS-ego is highlighted in blue.

No.	TARS	$\{\mathcal{L}_{seg}, \mathcal{L}_{ego}, \mathcal{L}_{opt}\}$	$\mathcal{L}_{bg}$ or $\lambda_{bg}$	Overall				Moving	Static
				EPE↓	AccS↑	AccR↑	RNE↓	MRNE↓	SRNE↓
1	no-ego	×	0.25	0.124	23.6	54.7	0.050	0.066	0.048
	no-ego	×	0.50	0.111	28.5	59.3	0.045	<b>0.065</b>	0.043
	no-ego	×	0.75	0.103	32.5	63.2	0.042	0.066	0.039
	no-ego	×	1.00	<b>0.098</b>	<b>34.3</b>	<b>65.8</b>	<b>0.040</b>	0.067	<b>0.036</b>
2	ego	✓	×	0.107	32.5	62.4	0.043	0.062	0.040
	ego	✓	0.50	<b>0.092</b>	<b>39.0</b>	<b>69.1</b>	<b>0.037</b>	<b>0.061</b>	<b>0.034</b>
3	ego	Decoder $\mathcal{N}_{TVF} = 5$		0.094	38.8	68.5	0.038	0.062	0.034
	ego	Decoder $\mathcal{N}_{TVF} = 9$		<b>0.092</b>	<b>39.0</b>	<b>69.1</b>	<b>0.037</b>	<b>0.061</b>	0.034
	ego	Decoder $\mathcal{N}_{TVF} = 13$		0.093	38.1	68.7	0.037	0.062	0.034

$\lambda_{bg}$  could cheat AccS&AccR as they reflect overall accuracy on the VOD dataset, where static points dominate the scene. However, it undermines the MRNE. We advocate emphasizing dynamic objects in radar scene flow, which is why we set  $\lambda_{bg} = 0.5$ . Group *No. 2*: we include the ego-motion head but firstly without  $\mathcal{L}_{bg}$ , which yields AccR of 62.4%. After enabling  $\mathcal{L}_{bg}$ , both moving and static points get improved. Group *No. 3*: we test the impact of  $\mathcal{N}_{TVF}$ . However, it did not lead to significant differences among the three setups, because each frame in the VOD dataset contains only 256 points, resulting in a highly sparse TVF.

## 5. Conclusion

We introduced TARS, a traffic-aware radar scene flow model. Leveraging traffic information from an object detector, TARS employs the traffic vector field encoder to build a holistic traffic-level scene understanding, and uses the TVF decoder to perceive the motion rigidity in traffic context. Quantitative results show that TARS notably exceeds SOTA accuracy on both the proprietary datasets and VOD dataset. Ablation studies highlight the effectiveness of key components in our design, such as incorporating OD feature maps, using a coarse-grid TVF, and applying global attention. Qualitative results demonstrate TARS’s ability to capture rigid motion and tangential movements.



## References

- [1] Nicolas Ballas, Li Yao, Chris Pal, and Aaron Courville. Delving deeper into convolutional networks for learning video representations. *arXiv preprint arXiv:1511.06432*, 2015. 4, 5
- [2] Geonho Bang, Kwangjin Choi, Jisong Kim, Dongsuk Kum, and Jun Won Choi. Radardistill: Boosting radar-based object detection performance via knowledge distillation from lidar features. In *Proceedings of the IEEE/CVF Conference on Computer Vision and Pattern Recognition*, pages 15491–15500, 2024. 6
- [3] Stefan Andreas Baur, David Josef Emmerichs, Frank Moosmann, Peter Pinggera, Björn Ommer, and Andreas Geiger. Slim: Self-supervised lidar scene flow and motion segmentation. In *Proceedings of the IEEE/CVF international conference on computer vision*, pages 13126–13136, 2021. 7
- [4] Aseem Behl, Despoina Paschalidou, Simon Donné, and Andreas Geiger. Pointflownet: Learning representations for rigid motion estimation from point clouds. In *Proceedings of the IEEE/CVF Conference on Computer Vision and Pattern Recognition*, pages 7962–7971, 2019. 2
- [5] Yukang Chen, Jianhui Liu, Xiangyu Zhang, Xiaojuan Qi, and Jiaya Jia. Voxelnext: Fully sparse voxelnet for 3d object detection and tracking. In *Proceedings of the IEEE/CVF Conference on Computer Vision and Pattern Recognition*, pages 21674–21683, 2023. 6
- [6] Wencan Cheng and Jong Hwan Ko. Bi-pointflownet: Bidirectional learning for point cloud based scene flow estimation. In *European Conference on Computer Vision*, pages 108–124. Springer, 2022. 2, 3
- [7] Jianning Deng, Gabriel Chan, Hantao Zhong, and Chris Xiaoxuan Lu. Robust 3d object detection from lidar-radar point clouds via cross-modal feature augmentation. In *2024 IEEE International Conference on Robotics and Automation (ICRA)*, pages 6585–6591. IEEE, 2024. 6
- [8] Fangqiang Ding, Zhijun Pan, Yimin Deng, Jianning Deng, and Chris Xiaoxuan Lu. Self-supervised scene flow estimation with 4-d automotive radar. *IEEE Robotics and Automation Letters*, 7(3):8233–8240, 2022. 2, 6, 7, 1, 5
- [9] Fangqiang Ding, Andras Palffy, Dariu M Gavrilă, and Chris Xiaoxuan Lu. Hidden gems: 4d radar scene flow learning using cross-modal supervision. In *Proceedings of the IEEE/CVF Conference on Computer Vision and Pattern Recognition*, pages 9340–9349, 2023. 2, 5, 6, 7, 1, 3, 4
- [10] Fangqiang Ding, Zhen Luo, Peijun Zhao, and Chris Xiaoxuan Lu. milliflow: Scene flow estimation on mmwave radar point cloud for human motion sensing. In *European Conference on Computer Vision*, pages 202–221. Springer, 2024. 2
- [11] Guanting Dong, Yueyi Zhang, Hanlin Li, Xiaoyan Sun, and Zhiwei Xiong. Exploiting rigidity constraints for lidar scene flow estimation. In *Proceedings of the IEEE/CVF Conference on Computer Vision and Pattern Recognition*, pages 12776–12785, 2022. 1, 2
- [12] Fabian Duffhauss and Stefan A Baur. Pillarflownet: A real-time deep multitask network for lidar-based 3d object detection and scene flow estimation. In *2020 IEEE/RSJ International Conference on Intelligent Robots and Systems (IROS)*, pages 10734–10741. IEEE, 2020. 2
- [13] Emeç Erçelik, Ekim Yurtsever, Mingyu Liu, Zhijie Yang, Hanzhen Zhang, Pınar Topçam, Maximilian Listl, Yılmaz Kaan Caylı, and Alois Knoll. 3d object detection with a self-supervised lidar scene flow backbone. In *European Conference on Computer Vision*, pages 247–265. Springer, 2022. 2
- [14] Hehe Fan and Yi Yang. Pointrnn: Point recurrent neural network for moving point cloud processing. *arXiv preprint arXiv:1910.08287*, 2019. 5
- [15] Zan Gojcic, Or Litany, Andreas Wieser, Leonidas J Guibas, and Tolga Birdal. Weakly supervised learning of rigid 3d scene flow. In *Proceedings of the IEEE/CVF conference on computer vision and pattern recognition*, pages 5692–5703, 2021. 1, 2, 4
- [16] Xiaodong Gu, Chengzhou Tang, Weihao Yuan, Zuozhuo Dai, Siyu Zhu, and Ping Tan. Rcp: Recurrent closest point for point cloud. In *Proceedings of the IEEE/CVF Conference on Computer Vision and Pattern Recognition*, pages 8216–8226, 2022. 1
- [17] Shengyu Huang, Zan Gojcic, Jiahui Huang, Andreas Wieser, and Konrad Schindler. Dynamic 3d scene analysis by point cloud accumulation. In *European Conference on Computer Vision*, pages 674–690. Springer, 2022. 1, 2
- [18] Wolfgang Kabsch. A solution for the best rotation to relate two sets of vectors. *Acta Crystallographica Section A: Crystal Physics, Diffraction, Theoretical and General Crystallography*, 32(5):922–923, 1976. 2, 1
- [19] Ishan Khatri, Kyle Vedder, Neehar Peri, Deva Ramanan, and James Hays. I can’t believe it’s not scene flow! In *European Conference on Computer Vision*, pages 242–257. Springer, 2025. 3, 6
- [20] Jaeyeul Kim, Jungwan Woo, Ukcheol Shin, Jean Oh, and Sunghoon Im. Flow4d: Leveraging 4d voxel network for lidar scene flow estimation. *IEEE Robotics and Automation Letters*, 2025. 2, 7
- [21] Yair Kittenplon, Yonina C Eldar, and Dan Raviv. Flow-step3d: Model unrolling for self-supervised scene flow estimation. In *Proceedings of the IEEE/CVF Conference on Computer Vision and Pattern Recognition*, pages 4114–4123, 2021. 2, 7, 3
- [22] Alex H Lang, Sourabh Vora, Holger Caesar, Lubing Zhou, Jiong Yang, and Oscar Beijbom. Pointpillars: Fast encoders for object detection from point clouds. In *Proceedings of the IEEE/CVF conference on computer vision and pattern recognition*, pages 12697–12705, 2019. 2, 3
- [23] Itai Lang, Dror Aiger, Forrester Cole, Shai Avidan, and Michael Rubinstein. Scoop: Self-supervised correspondence and optimization-based scene flow. In *Proceedings of the IEEE/CVF Conference on Computer Vision and Pattern Recognition*, pages 5281–5290, 2023. 2
- [24] Ruibo Li, Chi Zhang, Guosheng Lin, Zhe Wang, and Chunhua Shen. Rigidflow: Self-supervised scene flow learning on point clouds by local rigidity prior. In *Proceedings of the IEEE/CVF Conference on Computer Vision and Pattern Recognition*, pages 16959–16968, 2022. 1, 2

- [25] Yancong Lin and Holger Caesar. Icp-flow: Lidar scene flow estimation with icp. In *Proceedings of the IEEE/CVF Conference on Computer Vision and Pattern Recognition*, pages 15501–15511, 2024. [1](#), [2](#), [4](#)
- [26] Xingyu Liu, Charles R Qi, and Leonidas J Guibas. Flownet3d: Learning scene flow in 3d point clouds. In *Proceedings of the IEEE/CVF conference on computer vision and pattern recognition*, pages 529–537, 2019. [1](#), [2](#), [4](#), [3](#)
- [27] Zhe Liu, Jinghua Hou, Xinyu Wang, Xiaoqing Ye, Jingdong Wang, Hengshuang Zhao, and Xiang Bai. Lion: Linear group rnn for 3d object detection in point clouds. *Advances in Neural Information Processing Systems*, 37:13601–13626, 2024. [6](#)
- [28] Andras Palffy, Ewoud Pool, Srimannarayana Baratam, Julian FP Kooij, and Dariu M Gavrilă. Multi-class road user detection with 3+ 1d radar in the view-of-delft dataset. *IEEE Robotics and Automation Letters*, 7(2):4961–4968, 2022. [2](#), [6](#)
- [29] Zhijun Pan, Fangqiang Ding, Hantao Zhong, and Chris Xiaoxuan Lu. Ratrack: moving object detection and tracking with 4d radar point cloud. In *2024 IEEE International Conference on Robotics and Automation (ICRA)*, pages 4480–4487. IEEE, 2024. [6](#)
- [30] Charles Ruizhongtai Qi, Li Yi, Hao Su, and Leonidas J Guibas. Pointnet++: Deep hierarchical feature learning on point sets in a metric space. *Advances in neural information processing systems*, 30, 2017. [2](#), [3](#)
- [31] Patrik Vacek, David Hurých, Karel Zimmermann, and Tomáš Svoboda. Let-it-flow: Simultaneous optimization of 3d flow and object clustering. *IEEE Transactions on Intelligent Vehicles*, 2024. [2](#)
- [32] Kavisha Vidanapathirana, Shin-Fang Chng, Xueqian Li, and Simon Lucey. Multi-body neural scene flow. In *2024 International Conference on 3D Vision (3DV)*, pages 126–136. IEEE, 2024. [2](#)
- [33] Guangming Wang, Xinrui Wu, Zhe Liu, and Hesheng Wang. Hierarchical attention learning of scene flow in 3d point clouds. *IEEE Transactions on Image Processing*, 30:5168–5181, 2021. [2](#), [3](#), [4](#), [7](#), [8](#)
- [34] Huiyu Wang, Yukun Zhu, Bradley Green, Hartwig Adam, Alan Yuille, and Liang-Chieh Chen. Axial-deeplab: Stand-alone axial-attention for panoptic segmentation. In *European conference on computer vision*, pages 108–126. Springer, 2020. [5](#)
- [35] Yi Wei, Ziyi Wang, Yongming Rao, Jiwen Lu, and Jie Zhou. Pv-raft: Point-voxel correlation fields for scene flow estimation of point clouds. In *Proceedings of the IEEE/CVF conference on computer vision and pattern recognition*, pages 6954–6963, 2021. [2](#), [3](#)
- [36] Zhiqing Wei, Fengkai Zhang, Shuo Chang, Yangyang Liu, Huici Wu, and Zhiyong Feng. Mmwave radar and vision fusion for object detection in autonomous driving: A review. *Sensors*, 22(7):2542, 2022. [1](#)
- [37] Benjamin Wilson, William Qi, Tanmay Agarwal, John Lambert, Jagjeet Singh, Siddhesh Khandelwal, Bowen Pan, Ratnesh Kumar, Andrew Hartnett, Jhony Kaesemodel Pontes, et al. Argoverse 2: Next generation datasets for self-driving perception and forecasting. *arXiv preprint arXiv:2301.00493*, 2023. [2](#)
- [38] Sanghyun Woo, Jongchan Park, Joon-Young Lee, and In So Kweon. Cbam: Convolutional block attention module. In *Proceedings of the European conference on computer vision (ECCV)*, pages 3–19, 2018. [5](#), [1](#)
- [39] Wenxuan Wu, Zhi Yuan Wang, Zhuwen Li, Wei Liu, and Li Fuxin. Pointpwc-net: Cost volume on point clouds for (self-) supervised scene flow estimation. In *Computer Vision—ECCV 2020: 16th European Conference, Glasgow, UK, August 23–28, 2020, Proceedings, Part V 16*, pages 88–107. Springer, 2020. [1](#), [2](#), [3](#), [4](#), [7](#)
- [40] Qingwen Zhang, Yi Yang, Heng Fang, Ruoyu Geng, and Patric Jensfelt. DeFlow: Decoder of scene flow network in autonomous driving. In *2024 IEEE International Conference on Robotics and Automation (ICRA)*, pages 2105–2111, 2024. [2](#), [7](#), [3](#)
- [41] Zaiwei Zhang, Bo Sun, Haitao Yang, and Qixing Huang. H3dnet: 3d object detection using hybrid geometric primitives. In *Computer Vision—ECCV 2020: 16th European Conference, Glasgow, UK, August 23–28, 2020, Proceedings, Part XII 16*, pages 311–329. Springer, 2020. [2](#)
- [42] Yi Zhou, Lulu Liu, Haocheng Zhao, Miguel López-Benítez, Limin Yu, and Yutao Yue. Towards deep radar perception for autonomous driving: Datasets, methods, and challenges. *Sensors*, 22(11):4208, 2022. [3](#)

# TARS: Traffic-Aware Radar Scene Flow Estimation

## Supplementary Material

### A. Experiment Details

#### A.1. Further Model Details

In this section we provide more details about TARS.

When computing the point-level flow embeddings in Sec. 3.2.1, we use an MLP for positional encoding but omit it in those equations for simplicity. It is also applied in cross-attention in the TVF decoder (Sec. 3.4).

In the scene update stage in Sec. 3.3, we firstly apply CNN layers to the feature map  $\chi_{od}^l \in \mathbb{R}^{H_l \times W_l \times D_l}$  to adapt the object features. We then apply pooling layers, because feature maps from the OD pyramid have varying resolutions ( $H_l, W_l$ ) at each level, and we match them with the pre-defined shape of the coarse TVF.

In the flow painting stage in Sec. 3.3, we fuse the scene  $\mathbf{X}_{\text{traffic}}^l$  and motion feature  $\mathbf{X}_{\text{motion}}^l$  in a spatial attention style [38], specifically:

$$\mathbf{X}_{\text{fusion}}^l = \mathbf{w}^l \odot \mathbf{X}_{\text{traffic}}^l + (1 - \mathbf{w}^l) \odot \mathbf{X}_{\text{motion}}^l, \quad \text{with} \quad (10)$$

$$\mathbf{w}^l = \sigma(\text{Concat}(\mathbf{W}_1 * \mathbf{X}_{\text{traffic}}^l, \mathbf{W}_2 * \mathbf{X}_{\text{motion}}^l)), \quad (11)$$

where  $\mathbf{W}_1, \mathbf{W}_2$  are CNN kernels that generate pixel-wise attention scores,  $\mathbf{w}^l$  is the pixel-wise attention weights.

In the flow painting stage in Sec. 3.3, we use axial attention to provide the global receptive field, specifically:

$$\text{TVF}_{\tau}^l = \text{TVF}_{\tau}^l - \mathbf{H} + \text{TVF}_{\tau}^l - \mathbf{W}, \quad \text{with} \quad (12)$$

$$\text{TVF}_{\tau}^l - \mathbf{H} = \text{Self-A}(\text{Col}(\text{TVF}_{\tau-1}^l)), \quad (13)$$

$$\text{TVF}_{\tau}^l - \mathbf{W} = \text{Self-A}(\text{Row}(\text{TVF}_{\tau}^l - \mathbf{H})), \quad (14)$$

$$\text{Self-A}(\cdot) = \text{Attention}(\cdot, \cdot, \cdot), \quad (15)$$

where  $\tau = \{1, \dots, \omega\}$ ,  $\text{Col}(\cdot)$  collects  $\mathbf{W}$  column vectors and  $\text{Row}(\cdot)$  collects  $\mathbf{H}$  row vectors from the 2D TVF.

On the proprietary dataset, we provide **all** models with ego-motion  $\Omega \in \mathbb{R}^{4 \times 4}$  as known input. We apply ego-motion compensation before the PointGRU blocks (Sec. 3.5), aligning  $O$  and  $P$ , as well as  $P$  and  $Q$  into the same coordinate system.

#### A.2. Details of Ego-motion head

On the VOD dataset, our TARS-ego adopts the same approach as RaFlow and CMFlow [8, 9] to train an ego-motion head. It predicts the ego transformation, which is treated as static flow and assigned to all static points. This assignment requires our model to distinguish between moving and static points, which is achieved by a motion-segmentation head.

**Motion-segmentation head.** The motion-segmentation head takes the final flow embeddings from the  $L$ -th level

of TARS-ego as input and outputs a probability map  $\mathbf{S}$  indicating for each point whether it is moving or static. We use a simple three-layer MLP followed by a sigmoid function to generate the probability map. A binary segmentation mask can be generated from  $\mathbf{S}$  using a threshold of 0.5.

We apply the same training strategy in previous works [8, 9]. During training, we use ground truth (GT) segmentation pseudo-labels as the segmentation mask, in order to provide stable segmentation results for training the ego-motion head. During testing, we use the model output from the motion-segmentation head.

**Ego-motion head.** Since  $P_{\text{warp}}$  is obtained by warping  $P$  using the scene flow output  $F^L$  from the last  $L$ -th level, they can be used as natural correspondences to infer the ego motion. In the ego-motion head, we take  $P, P_{\text{warp}}$ , and  $\mathbf{S}$  as input. Then we perform the differentiable weighted Kabsch algorithm [18], which infers rigid transformation between  $P$  and  $P_{\text{warp}}$ , with  $(1 - \mathbf{S})$  as the point weight to neglect moving points. Finally, we use the binary motion segmentation mask generated from  $\mathbf{S}$  to identify static points and assign the inferred ego-motion to static points as their final scene flow  $F_{\text{bg}}$ . Since the ego-motion is inferred between  $P$  and  $P_{\text{warp}}$ , a more accurate  $F^L$  leads to improved ego-motion predictions and, ultimately, more accurate static flow  $F_{\text{bg}}$ .

#### A.3. TARS-ego and TARS-superego

On the VOD dataset, we evaluate our model using two setups that apply the ego-motion information differently: TARS-ego and TARS-superego, results shown in Tab. 2 of the main manuscript. TARS-ego uses GT ego-motion to train a ego-motion head and motion-segmentation head to refine the static flow  $F_{\text{bg}}$ ; while TARS-superego uses ego-motion as input and applies ego-motion compensation, expecting the static flow  $F_{\text{bg}}$  to be zero vectors (without those additional heads). On the proprietary dataset, since ego-motion compensation is applied to **all** models, we do not specifically label our model as TARS-superego. In this section, we discuss the reason of leveraging ego-motion.

On one hand, ego-motion information from an odometer is simple, easy to obtain, yet highly effective. Utilizing this information enhances scene flow performance in both ways: as supervision signal for an ego-motion head, or as known input for ego-motion compensation. Nevertheless, the latter aligns more closely with real-world autonomous driving scenarios, where a GPS/IMU sensor is often available. It helps address the challenges of radar scene flow.

On the other hand, performing ego-motion compensation maximizes the potential of our model TARS. By compensating point cloud  $P$  into the coordinate system of point

cloud  $Q$ , the points in  $P$  and the OD feature map from  $Q$  share a common coordinate system starting from the lowest level of TARS. This eliminates the need for the lower levels of TARS to firstly warp the points in  $P$  closer to the corresponding object features, ensuring alignment within the TVF throughout the process.

#### A.4. Details of Reproduced LiDAR Models

For a complete comparison with prior works, we include latest LiDAR scene flow models [20, 40] in the comparison on the VOD dataset, results shown in Tab. 2 in the main manuscript. In this section, we provide the details of our reproduction of DeFlow [40] and Flow4D [20].

DeFlow and Flow4D underperform compared to TARS and CMFlow [9]. This is because their fully-voxel representation, designed for the efficiency challenge in large-scale LiDAR point clouds, become unsuitable for sparse radar point clouds. In DeFlow [40], the GRU-based voxel-to-point refinement module becomes ineffective, because most pillars contain only a few radar point, leading to loss of precise location (although this effectively improves the efficiency). Similarly, Flow4D [20]’s fine-grain 4D voxel representation is less appropriate for sparse radar data.

Originally implemented on the LiDAR dataset Argoverse 2 [37], DeFlow and Flow4D take two LiDAR point clouds  $P \in \mathbb{R}^{N \times 3}$  and  $Q \in \mathbb{R}^{M \times 3}$  as input. Note that, both of them take only  $x, y, z$  coordinates as input channels, without using the intensity information from LiDAR. For fair comparison on the VOD dataset, we extend their input to 5 dimensions, adding RRV (relative radial velocity) and RCS (radar cross-section). We also adapt their grid feature map shape according to VOD’s point cloud range.

Flow4D supports multi-frame input, while its 2-frame setup also achieves SOTA performance on Argoverse 2. As labeled in Tab. 2, we test the Flow4D-2frame setup for a fair comparison with other models.

During training, we use the following losses:  $\mathcal{L}_{sc}$ ,  $\mathcal{L}_{ss}$ ,  $\mathcal{L}_{rd}$ ,  $\mathcal{L}_{fg}$ , and  $\mathcal{L}_{bg}$  (details see Appendix D.2). We keep their original implementations, and since these models lack ego-motion heads, we omit TARS-ego & CMFlow’s additional losses ( $\mathcal{L}_{seg}$ ,  $\mathcal{L}_{ego}$ ,  $\mathcal{L}_{opt}$ ). This setup is the same as the training of our TARS-no-ego model, where we also removed the ego-motion and motion-segmentation head (results shown in Tab. 5 Group No. 1, highlighted in blue). Certainly, ego-motion compensation is also not applied for TARS-no-ego. Under the same training loss and “no-ego” setup, DeFlow and Flow4D still have a large accuracy gap compared to TARS-no-ego (16.7% and 18.5% on AccS; 27.7% and 33.1% on AccR, respectively).

#### A.5. Training Strategy of Dual-task Network

TARS jointly perform object detection and radar scene flow, enhancing the scene flow accuracy and also enabling a com-

prehensive perception. Experiments in PillarFlowNet [12] show that joint training of these two tasks reduces the performance of each individual task. Our experimental results of joint training are consistent with theirs, shown in Tab. A. Therefore, we perform a staged training: first train an object detector, then freeze its parameters to stabilize feature maps for the scene flow branch. This maintains OD performance while also allowing flexibility to adopt different training strategies for the object detector.

Table A. Joint training experiment on the proprietary dataset.

Training Strategy			Scene Flow Branch				OD Branch AP [%]↑			
OD pre-trained	Joint	Staged	MEPE↓	AccS↑	AccR↑	SEPE↓	Car	Ped.	Cycl.	Truck
no			0.094	60.4	77.0	<b>0.026</b>	65.3	51.7	55.4	52.3
yes, not frozen	✓		<b>0.067</b>	66.8	<b>87.1</b>	0.036	66.7	53.2	60.0	53.8
yes, frozen		✓	0.069	<b>69.8</b>	86.8	0.038	<b>67.5</b>	<b>54.5</b>	<b>62.2</b>	<b>55.9</b>

#### A.6. Object Detection Branch Details

We use an off-the-shelf object detector as the OD branch on both datasets and freeze its weights. In this way, we maintain the OD performance and stabilize the feature map. As discussed in Sec. 3.1, the object detection branch should have a grid-based backbone to provide bird’s eye view (BEV) feature maps to the scene flow branch. This excludes point-based detectors, such as 3D-SSD [41], where features are preserved in point form rather than being structured into grids. In contrast, voxel-based detectors typically generate multi-scale feature maps, which aligns well with TARS’s hierarchical architecture. Therefore, we utilize the OD feature map at each corresponding level within our hierarchical design.

We employ PointPillars [22] as the object detector on the VOD dataset (result shown in Tab. B). The OD branch result on the proprietary dataset is shown in Tab. C.

Table B. Performance of the object detection branch on the VoD dataset. The results are reported separately for the entire annotated area and the driving corridor area.

Dataset	AP in the entire annotated area [%]↑				AP in the driving corridor area [%]↑			
	Car	Pedestrian	Cyclist	mAP	Car	Pedestrian	Cyclist	mAP
VOD	30.59	30.21	61.95	40.92	64.19	41.61	85.04	63.61

Table C. Performance of the OD branch on the proprietary dataset.

Dataset	AP in the entire annotated area [%]↑			
	Car	Pedestrian	Cyclist	Truck
proprietary	67.46	54.50	62.15	55.86

## B. Additional Ablation Study

### B.1. Ablation study of OD branch

In Tab. D, we test the effect of the object detection branch’s accuracy on the performance of the scene flow branch. By



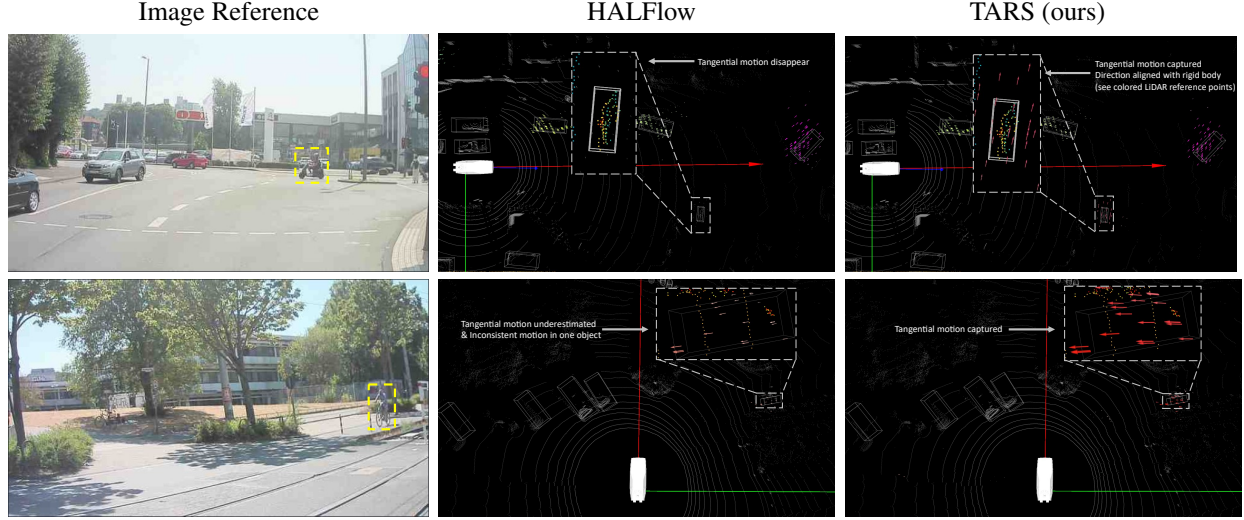


Figure 7. Qualitative results on the proprietary dataset, compared with HALFlow [33]. It illustrates two scenarios about vulnerable road users approaching the front area of the ego vehicle with tangential motion. TARS is able to capture these challenging tangential movements.

adjusting the feature channels of PointPillars, we create three models of varying sizes: PP-L, PP-M, and PP-S (from large to small).

However, we observed that even with massive reductions in feature channels and parameters, PP-M and PP-S still maintain OD accuracy comparable to PP-L, and their corresponding scene flow branch performance is also similar. To isolate the corrective effect of the ego-motion head on scene flow predictions, we further test the performance of TARS-no-ego under three PointPillars setups. The experiments show that using PP-L achieves the best performance in both TARS-ego and TARS-no-ego models. However, due to the similar accuracy of the OD branch, the performance differences in the scene flow branch are not significant.

Table D. Ablation study of the OD branch on the VOD dataset. PP-S, PP-M, PP-L refer to three different PointPillars [22] setups. TARS-no-ego: without ego-motion head and three supervision signals  $\mathcal{L}_{\{\text{seg, ego, opt}\}}$ .

Model	#Params	Object Detection branch				Scene Flow Branch								
		AP in the entire annotated area				TARS-ego			TARS-no-ego					
		Car	Ped.	Cycl.	mAP	EPE	AccR	AccS	EPE	AccR	AccS	EPE	AccR	AccS
PP-S	<b>0.05M</b>	25.63	28.64	61.04	38.44	0.093	38.1	68.5	0.117	27.0	57.4			
PP-M	0.33M	29.73	27.28	59.33	38.78	0.095	37.1	67.2	0.114	27.9	58.3			
PP-L	9.30M	<b>30.59</b>	<b>30.21</b>	<b>61.95</b>	<b>40.92</b>	<b>0.092</b>	<b>39.0</b>	<b>69.1</b>	<b>0.111</b>	<b>28.5</b>	<b>59.3</b>			

## B.2. Class-wise Scene Flow Evaluation

Khatri et al. [19] proposed a novel scene flow evaluation method, computing class-aware EPE to analyze the failure cases in scene flow. We provide this analysis in Tab. E for the best three models in the VOD dataset, i.e. DeFlow [40], CMFlow [9] and our TARS-ego. Note that, Here we adapt the Bucket Normalized EPE [19] to MRNE. The reason is that, on the VOD dataset we compute MRNE for dynamic

points, while EPE is an overall metric for all points. Therefore, to achieve class-aware evaluation, we compute per-class MRNE.

Table E. Scene flow evaluation on the VOD dataset, with per-class MRNE analysis. “Sup.”: supervision.

Method	Sup.	Overall				Moving	Static	Per-class MRNE↓		
		EPE↓	AccS↑	AccR↑	RNE↓	MRNE↓	SRNE↓	Car	Ped.	Cycl.
DeFlow [40]	Cross	0.217	11.8	31.6	0.087	0.098	0.085	0.092	0.081	0.106
CMFlow [9]	Cross	0.130	22.8	53.9	0.052	0.072	0.049	0.064	0.062	0.086
TARS-ego (ours)	Cross	<b>0.092</b>	<b>39.0</b>	<b>69.1</b>	<b>0.037</b>	<b>0.061</b>	<b>0.034</b>	<b>0.051</b>	<b>0.052</b>	<b>0.073</b>

Table F. Comparison with fully-supervised models on the VOD dataset. Fully-supervised model results are cited from [9]. “Sup.” indicates the supervision signal, Full: training with actual scene flow ground truth, Self: training with only self-supervised losses, Cross: with additional cross-modal losses.

Method	Sup.	EPE [m]↓	AccS [%]↑	AccR [%]↑	RNE [m]↓
FlowStep3D [21]	Full	0.286	6.1	18.5	0.115
Bi-PointFlowNet [6]	Full	0.242	16.4	35.0	0.097
FlowNet3D [26]	Full	0.201	16.9	37.9	0.081
PointPWC-Net [39]	Full	0.196	17.7	39.7	0.079
PV-RAFT [35]	Full	<b>0.126</b>	<b>25.8</b>	<b>58.7</b>	<b>0.051</b>
PointPWC-Net [39]	Self	0.422	2.6	11.3	0.169
FlowStep3D [21]	Self	0.292	3.4	16.1	0.117
CMFlow [9]	Cross	<b>0.141</b>	<b>22.8</b>	<b>53.9</b>	<b>0.052</b>
TARS-ego (ours)	Cross	<b>0.092</b>	<b>39.0</b>	<b>69.1</b>	<b>0.037</b>

## B.3. Comparison with Fully-supervised Methods

Ding et al. [9] compared weakly-supervised CMFlow with fully-supervised LiDAR models, e.g. PV-RAFT [35]. We continue this discussion in Tab. F. Note that “fully-supervised” refers to training with actual scene flow GT derived from human-annotated bounding boxes and tracking IDs. In contrast, the aforementioned pseudo scene flow

GT  $\hat{F}_{fg}$  in the foreground loss is generated using an off-the-shelf, pre-trained LiDAR multi-object tracking model, requiring no additional annotation efforts.

Experiments in [9] demonstrated that the weakly-supervised CMFlow (with cross-modal losses) achieved 3% lower AccS and 4.8% lower AccR compared to the fully-supervised PV-RAFT. Nevertheless, CMFlow was able to achieve comparable EPE and AccR to the fully-supervised PV-RAFT by leveraging extra weakly-supervised training samples without costly annotations ( $\sim 140\%$  more than the number of training samples used for PV-RAFT). In contrast, as shown in Tab. F, TARS-ego surpasses fully-supervised PV-RAFT with a 13.2% higher AccS and 10.4% higher AccR, without requiring any additional training samples.

#### B.4. Concerns about Emergency

In TARS, perceiving traffic is one of the core ideas. Incorporating traffic modeling into motion prediction may raise concerns about emergent situations, such as a pedestrian suddenly entering traffic. Nevertheless, this is addressed by the overall design of TARS: all traffic-related modules in TARS employ attentive layers, enabling the neural network to adaptively balance the reliance on point-level and traffic-level features.

This is particularly evident in the encoding and decoding processes of the TVF. In the TVF encoder, we treat the point property  $\mathbf{p}^{l-1}$  (from PointNet) and motion features  $\mathbf{e}^{l-1}$  (flow embeddings) as equally important by concatenating them and then applying point-to-grid self-attention. Similarly, in the TVF decoder, we form the query by concatenating  $\mathbf{p}^l$  with the upsampled  $\mathbf{e}^{l-1}$  for grid-to-point cross-attention with the TVF.

More importantly, we leverage additional information from the OD branch, which provides object features of vulnerable road users. This helps the scene flow branch in perceiving the presence of vulnerable road users.

In Fig. 7, we show two scenarios where a person riding a bike approaches the front area of the ego vehicle from a tangential direction, which is particularly challenging to perceive by radar sensors. Our TARS successfully captures the tangential motion of the bike, while, in the outputs of the previous work, the tangential motion erroneously disappears or is underestimated.

These examples also highlights the importance of combining radar scene flow with object detection in autonomous driving. By integrating motion prediction with object bounding boxes, the system can select the optimal strategy based on the ego vehicle’s speed and the direction and magnitude of target’s motion.

#### C. Efficiency Analysis

We compare the efficiency of TARS with the previous best models on both datasets. All experiments are conducted on

Table G. Efficiency analysis on the VOD dataset. The total runtime is a sum of scene flow branch (SF) and OD branch (if exist). #Param: the number of parameters in the scene flow branch.

Method	Performance (VOD)			Runtime [ms]↓			#Param ↓
	EPE [m]↓	AccS [%]↑	AccR [%]↑	Total	SF	OD	
CMFlow [9]	0.130	22.8	53.9	69	69	/	4.23M
TARS-ego (ours)	0.092	39.0	69.1	84	79	5	3.82M

Table H. Efficiency analysis on the proprietary dataset. The total runtime is a sum of scene flow branch (SF) and OD branch.

Method	Performance (proprietary)			Runtime [ms]↓			#Param ↓
	MEPE [m]↓	AccS [%]↑	AccR [%]↑	Total	SF	OD	
HALFlow [33]	0.170	50.9	63.8	77	77	/	1.00M
TARS (ours)	0.069	69.8	86.8	102	96	6	1.60M

a single GeForce RTX 3090 GPU with a batch size of 1.

As shown in Tab. G, on the VOD dataset, our scene flow branch has 3.82M parameters, which is fewer than CMFlow’s 4.23M. The total runtime per frame of TARS-ego is 84ms, 15ms higher than CMFlow’s 69ms, with 10ms attributed to the scene flow branch and 5ms to the additional OD branch. Nevertheless, TARS can achieve real-time performance under a 10-Hz radar, functioning as a unified system for both object detection and scene flow estimation.

The results on the proprietary dataset are shown in Tab. H. Compared to the previous best model, i.e., HALFlow, TARS adds 0.6M additional parameters. The total runtime of TARS is 102ms per frame, 25ms higher than HALFlow’s 77ms, with 19ms from the scene flow branch and 6ms from the additional OD branch. On the proprietary dataset, TARS operates at the edge of the real-time criterion and could achieve a real-time dual-task system with slight runtime optimization (e.g. using FP16).

TARS has a higher runtime on the proprietary dataset compared to the VOD dataset. This results from the significantly larger number of radar points per frame ( $\sim 6K$  vs. 256 points), and scene flow estimation operates on two input point clouds at the same time. On the VOD dataset, the increase in parameters is mainly due to the CNN layers for adapting the OD features in the TVF encoder.

#### D. Evaluation Metric & Loss Function

##### D.1. Evaluation Metrics

In this section, we introduce details of the evaluation metrics used in the experiments. Our input consists of two point clouds  $P$  and  $Q$ . Let  $\hat{\mathbf{f}}_i$  and  $\mathbf{f}_i$  represent the GT and predicted scene flow for a point  $p_i$ , respectively.  $N_{fg}$  and  $N_{bg}$  denote the number of moving points and static points. The subscripts fg or bg indicate points belonging to moving or static point set.

On the VOD dataset, we follow the evaluation metrics used in CMFlow [9]:

- $EPE = \frac{1}{N} \sum_{i=1}^N \|\mathbf{f}_i - \hat{\mathbf{f}}_i\|_2$ ,

- $\text{AccS} = \frac{1}{N} \sum_{i=1}^N \mathbb{I}(\text{EPE}_i < 0.05)$ ,
- $\text{AccR} = \frac{1}{N} \sum_{i=1}^N \mathbb{I}(\text{EPE}_i < 0.1)$ ,
- $\text{RNE} = \frac{1}{N} \sum_{i=1}^N \text{EPE}_i / \frac{r_{Ri}}{r_{Li}}$ , RNE is the EPE divided by the resolution ratio between radar and LiDAR, in order to accomodate low-resolution radar. The average resolution ratio is 2.5.
- $\text{MRNE} = \frac{1}{N_{\text{fg}}} \sum_{i \in P_{\text{fg}}} \text{RNE}_i$ ,
- $\text{SRNE} = \frac{1}{N_{\text{bg}}} \sum_{i \in P_{\text{bg}}} \text{RNE}_i$ ,

where  $\mathbb{I}(\cdot)$  is the indicator function, which evaluates to one if and only if the condition is true,  $\frac{r_R}{r_L}$  is the resolution ratio between radar and LiDAR.

On the proprietary dataset, high-resolution radars eliminate the need for RNE, and we focus on the evaluation of moving points since ego-motion compensation is applied:

- $\text{MEPE} = \frac{1}{N_{\text{fg}}} \sum_{i \in P_{\text{fg}}} \|\mathbf{f}_i - \hat{\mathbf{f}}_i\|_2$ ,
- $\text{MagE} = \frac{1}{N_{\text{fg}}} \sum_{i \in P_{\text{fg}}} \left| \|\mathbf{f}_i\|_2 - \|\hat{\mathbf{f}}_i\|_2 \right|$ ,
- $\text{DirE} = \frac{1}{N_{\text{fg}}} \sum_{i \in P_{\text{fg}}} \arccos \left( \frac{\mathbf{f}_i^T \cdot \hat{\mathbf{f}}_i}{\|\mathbf{f}_i\|_2 \|\hat{\mathbf{f}}_i\|_2} \right)$ ,
- $\text{AccS} = \frac{1}{N_{\text{fg}}} \sum_{i \in P_{\text{fg}}} \mathbb{I}(\text{MEPE}_i < 0.05)$ ,
- $\text{AccR} = \frac{1}{N_{\text{fg}}} \sum_{i \in P_{\text{fg}}} \mathbb{I}(\text{MEPE}_i < 0.1)$ ,
- $\text{SEPE} = \frac{1}{N_{\text{bg}}} \sum_{i \in P_{\text{bg}}} \|\mathbf{f}_i - \hat{\mathbf{f}}_i\|_2$ ,
- $\text{AvgEPE} = \frac{1}{2}(\text{MEPE} + \text{SEPE})$ ,

where  $\text{AccS}$  and  $\text{AccR}$  are computed only on moving points.  $\text{MagE}$  and  $\text{DirE}$  have not appeared in prior works. They reflect the two aspects of EPE: magnitude error and directional error. They can help reveal the sources of MEPE, e.g. high-speed underestimation or direction error.

## D.2. Weakly-supervised Training

In our weakly-supervised training, we employ the three self-supervised losses proposed in [8]: the soft Chamfer loss  $\mathcal{L}_{\text{sc}}$ , spatial smoothness loss  $\mathcal{L}_{\text{ss}}$ , and radial displacement loss  $\mathcal{L}_{\text{rd}}$ . We also use the foreground loss  $\mathcal{L}_{\text{fg}}$  [9] and our background loss  $\mathcal{L}_{\text{bg}}$ .

On the VOD dataset, we train TARS-ego with additional cross-modal losses from CMFlow [9]: the motion segmentation loss  $\mathcal{L}_{\text{seg}}$ , ego-motion loss  $\mathcal{L}_{\text{ego}}$ , optical flow loss  $\mathcal{L}_{\text{opt}}$ . TARS-superego and TARS-no-ego didn't use these losses.

Let  $P' = P_{\text{warp}}$  denote the resulting point cloud that warped by the predicted scene flow.

- The soft Chamfer loss  $\mathcal{L}_{\text{sc}}$  minimizes distances between nearest points between  $P_{\text{warp}}$  and  $Q$  while handling outliers using probabilistic matching, formulated as:

$$\begin{aligned} \mathcal{L}_{\text{sc}} = & \sum_{p'_i \in P_{\text{warp}}} \mathbb{I}(\nu(p'_i) > \delta) \left[ \min_{q_j \in Q} \|p'_i - q_j\|_2^2 - \epsilon \right]_+ \\ & + \sum_{q_i \in Q} \mathbb{I}(\nu(q_i) > \delta) \left[ \min_{p'_j \in P_{\text{warp}}} \|q_i - p'_j\|_2^2 - \epsilon \right]_+, \end{aligned} \quad (16)$$

where  $\nu(p)$  represents the per-point Gaussian density factor estimated using kernel density estimation, points with  $\nu(p)$  below threshold  $\delta$  are discarded as outliers, and the application of  $[\cdot]_+ = \max(0, \cdot)$  in Eq. (16) ensures that small matching discrepancies below  $\epsilon$  are ignored. For further details, we refer to RaFlow [8].

- The spatial smoothness loss  $\mathcal{L}_{\text{ss}}$  enforces neighboring points to have similar flow vectors, weighted by distance to ensure spatial smoothness, formulated as:

$$\mathcal{L}_{\text{ss}} = \sum_{p_i \in P} \sum_{p_j \in \mathcal{N}_P(p_i)} k(p_i, p_j) \|\mathbf{f}_i - \mathbf{f}_j\|_2^2, \quad (17)$$

where  $k(p_i, p_j) = \exp \left( -\frac{\|p_i - p_j\|_2^2}{\alpha} \right)$  is a radial basis function (RBF) kernel that weighs each neighbor point  $p_j \in \mathcal{N}_P(p_i)$  based on its Euclidean distance to  $p_i$ , with  $\alpha$  controlling the impact of the distance. All kernel weight values are normalized together using a softmax function.

- The radial displacement loss  $\mathcal{L}_{\text{rd}}$  constrains the radial projection of predicted flow vectors using RRV measurements, formulated as:

$$\mathcal{L}_{\text{rd}} = \sum_{p_i \in P} \left| \frac{\mathbf{f}_i^T \cdot p_i}{\|p_i\|} - \text{RRV}_i \Delta t \right|, \quad (18)$$

where  $p_i$  denotes the 3D point coordinate,  $\text{RRV}_i$  is the RRV measurement of a point, and  $\Delta t$  is the time interval between two radar scans.

- The foreground loss  $\mathcal{L}_{\text{fg}}^l$  uses pseudo scene flow GT  $\hat{F}_{\text{fg}}$  derived from the object bounding box and tracking ID generated by an off-the-shelf LiDAR multi-object tracking model. This loss is applied for each level and formulated as:

$$\mathcal{L}_{\text{fg}}^l = \frac{1}{N_{\text{fg}}^l} \sum_{i=1}^{N_{\text{fg}}^l} \left\| \hat{\mathbf{f}}_{\text{fg}_i}^l - \mathbf{f}_{\text{fg}_i}^l \right\|_2, \quad (19)$$

where  $\hat{\mathbf{f}}_{\text{fg}_i}^l$  is the pseudo GT for  $i$ -th moving point.

- The background loss  $\mathcal{L}_{\text{bg}}^l$  uses pseudo GT  $\hat{F}_{\text{bg}}$  derived from ego-motion or using zero vectors if ego-motion compensated, applied for level  $l$  and formulated as:

$$\mathcal{L}_{\text{bg}}^l = \frac{1}{N_{\text{bg}}^l} \sum_{i=1}^{N_{\text{bg}}^l} \left\| \hat{\mathbf{f}}_{\text{bg}_i}^l - \mathbf{f}_{\text{bg}_i}^l \right\|_2, \quad (20)$$

where  $\hat{\mathbf{f}}_{\text{bg}_i}^l$  is the pseudo GT for  $i$ -th static point.

- The overall loss  $\mathcal{L}_{\text{all}}$  is a sum of the above losses:

$$\mathcal{L}_{\text{all}} = \mathcal{L}_{\text{sc}} + \mathcal{L}_{\text{ss}} + \mathcal{L}_{\text{rd}} + \sum_{l=1}^L (\mathcal{L}_{\text{fg}}^l + \lambda_{\text{bg}} \mathcal{L}_{\text{bg}}^l). \quad (21)$$

On the VOD dataset, we use additional cross-modal losses [9]: the motion segmentation loss  $\mathcal{L}_{\text{seg}}$ , ego-motion loss  $\mathcal{L}_{\text{ego}}$ , optical flow loss  $\mathcal{L}_{\text{opt}}$ .

Table I. SOTA Object Detection and Tracking accuracy on the nuScenes and VOD dataset.

Sensor	nuScenes SOTA OD [%]↑		VOD SOTA OD [%]↑		SOTA Tracking [%]↑		
	Method	mAP	Method	mAP	Method	Dataset	AMOTA
LiDAR	LION (NeurIPS24) [27]	<b>69.8</b>	CMFA (ICRA24) [7]	<b>69.6</b>	VoxelNeXt (CVPR23) [5]	nuScenes	<b>71.0</b>
Radar	RadarDistill (CVPR24) [2]	20.5	CMFA (ICRA24) [7]	41.8	RaTrack (ICRA24) [29]	VOD	31.5

- The motion segmentation loss  $\mathcal{L}_{\text{seg}}$  uses the pseudo segmentation GT derived from the odometer and RRV to train a motion-segmentation head, formulated as:

$$\mathcal{L}_{\text{seg}} = \frac{1}{2} \sum_{i=1}^N \hat{s}_i \log(s_i) + (1 - \hat{s}_i) \log(1 - s_i), \quad (22)$$

where  $\hat{s}_i \in \{0, 1\}$  is the pseudo motion segmentation GT derived from odometer and RRV, and  $s_i \in [0, 1]$  is the predicted moving probability.

- The ego-motion loss  $\mathcal{L}_{\text{ego}}$  uses the GT ego-motion from the odometer to train an ego-motion head (Appendix A.2), formulated as:

$$\mathcal{L}_{\text{ego}} = \frac{1}{N} \sum_{i=1}^N \left\| (\Omega - \Omega_{\text{pred}}) \begin{bmatrix} p_i \\ 1 \end{bmatrix} \right\|_2, \quad (23)$$

where  $\Omega_{\text{pred}}$  is the predicted rigid transformation,  $\Omega$  is the GT ego-motion derived from odometry.

- The optical flow loss  $\mathcal{L}_{\text{opt}}$  projecting the scene flow onto an image and training with pseudo optical flow labels from an off-the-shelf optical flow model as additional supervision signal, formulated as:

$$\mathcal{L}_{\text{opt}} = \frac{1}{N_{\text{fg}}} \sum_{i=1}^{N_{\text{fg}}} D_{\text{Point-Ray}} \left( p_i + \mathbf{f}_i, \text{Ray}(p_i^{\text{proj}} + \widehat{\mathbf{f}}_i^{\text{opt}}, \theta) \right), \quad (24)$$

where  $p_i^{\text{proj}}$  is the projection of point  $p_i$  on the image plane,  $\widehat{\mathbf{f}}_i^{\text{opt}}$  is pseudo optical flow GT generated by a off-the-shelf image optical flow model, and  $D_{\text{Point-Ray}}(\cdot)$  calculates the point-line distance between the warped 3D point and the corresponding  $\text{Ray}(\cdot)$  traced from the optical flow-warped pixel. The parameter  $\theta$  denotes the sensor calibration parameters. This loss is computed only for moving points. For further details, we refer to [9].

## E. Discussion about Joint Network

TrackFlow [19] directly derives LiDAR scene flow from object detection and tracking result. This approach is intuitive, especially as it directly uses the bounding box from object detection to ensure motion rigidity. However, this method is unsuitable for radar, where sparsity and noise cause a 30-50 mAP drop in object detection (OD) and 40 AMOTA gap in tracking (see Tab. I). This results in missing motion predictions for false negatives and frequent tracking failures, severely limiting its ability to infer radar scene flow. In contrast, our point-wise radar scene flow predicts motion per

point, ensuring stable motion signals. Even if objects are undetected or noisily tracked, some moving points can still be identified, providing auxiliary information for decision-making in autonomous driving. In our design, TARS perceives traffic context by leveraging OD feature maps instead of bounding boxes, which reduces the reliance on OD accuracy (high recall).